We are IntechOpen, the world's leading publisher of Open Access books Built by scientists, for scientists

4,800
Open access books available

122,000
International authors and editors

135M
Downloads

Our authors are among the

154
Countries delivered to

TOP 1%
most cited scientists

12.2%
Contributors from top 500 universities

WEB OF SCIENCE™

Selection of our books indexed in the Book Citation Index in Web of Science™ Core Collection (BKCI)

Interested in publishing with us?
Contact book.department@intechopen.com

Numbers displayed above are based on latest data collected.
For more information visit www.intechopen.com

30

Electromagnetic Scattering Analysis of Simple Targets Embedded in Planar Multilayer Structures: Remote Sensing Applications

Sidnei J. S. Sant'Anna[1,2], J. C. da S. Lacava[2] and David Fernandes[2]
[1]*Instituto Nacional de Pesquisas Espaciais*
[2]*Instituto Tecnológico de Aeronáutica*
Brazil

1. Introduction

The potential and usefulness of SAR (Synthetic Aperture Radar) data for land uses and land cover change applications have been demonstrated over the past few decades. More recently, polarimetric SAR data have been widely used in electromagnetic modeling and inverse problems. Moreover, the combined use of numerical modeling and inversion methods has enabled computerized quantitative information extraction of the polarimetric data. In particular, the electromagnetic modeling can be used to increase the knowledge of non-metallic target reflectivity. The problem of detecting the many types of non-metallic land mines in the presence of widely varying soil background is an example of one of the most difficult subsurface sensing problems.

The target electromagnetic scattering characterization (van Zyl et al., 1987; Cloude & Pottier, 1996; Freeman & Durden, 1998; Sant'Anna et al., 2007a) might influence some remote sensing practical applications, as SAR image classification, sensor calibration among others. Consequently, understanding the target scattering mechanism plays a valuable role in the analysis and interpretation of polarimetric SAR data. In order to improve the insight into scattering mechanism subject, several electromagnetic models have been proposed in literature (Lin & Sarabandi, 1999; Israelsson et al., 2000; Zurk et al., 2001). Usually, in these models complex targets are modeled by a collection of targets having simple and canonical geometries. For instance, a three can have its elementary parts as trunk, branches and leaves, built through a set of dielectric cylinders and discs. Besides, depending on the modeling the simple targets have different sizes, shapes, orientations and dielectric properties. Therefore, the study of electromagnetic scattering of simple targets is fundamental to enhance the comprehension of the electromagnetic characteristics of more complex ones.

Keeping this issue in mind, the purpose of this work is to show the potentiality and applicability of an electromagnetic model within remote sensing subject. This modeling is based on scattering elements embedded in a multilayer planar structure, which is illuminated by an elliptically polarized plane wave at oblique incidence. Therefore, the chapter is organized as follow. In Section 2, the multilayer structure under analysis is

described jointly with an explanation of the electromagnetic modeling employed to solve the scattering problem. The electromagnetic model usefulness is illustrated in Section 3, through some remote sensing applications. The Section 4 is devoted to draw the conclusions concerning the obtained results.

2. Electromagnetic Model

The electromagnetic model is based on the determination of the electromagnetic fields scattered by a multilayer planar structure that is excited by plane waves. The structure under analysis is composed of N+2 isotropic, linear and homogenous layers stacked up in z direction. The layers are assumed to be unbounded along the x and y directions. The lower layer, having complex permittivity ε_g and complex permeability μ_g, is denoted as ground layer and occupies the negative-z region. The next N layers are characterized by thickness ℓ_n, complex permittivity ε_n and complex permeability μ_n, where $1 \le n \le N$. The planar interface $z = d_N$ separates the N-th layer from free space (the upper layer). Elements supporting electric (***J***) or magnetic (***M***) surface current densities are printed at arbitrary positions on each one of the N+1 interfaces of the structure. These elements will behave as scattering elements. The development is based on a global right-handed rectangular coordinate system located on the top of the ground layer (interface $z = 0$) and lying on the xy-plane. The geometry of the planar multilayer structure is depicted in Figure 1.

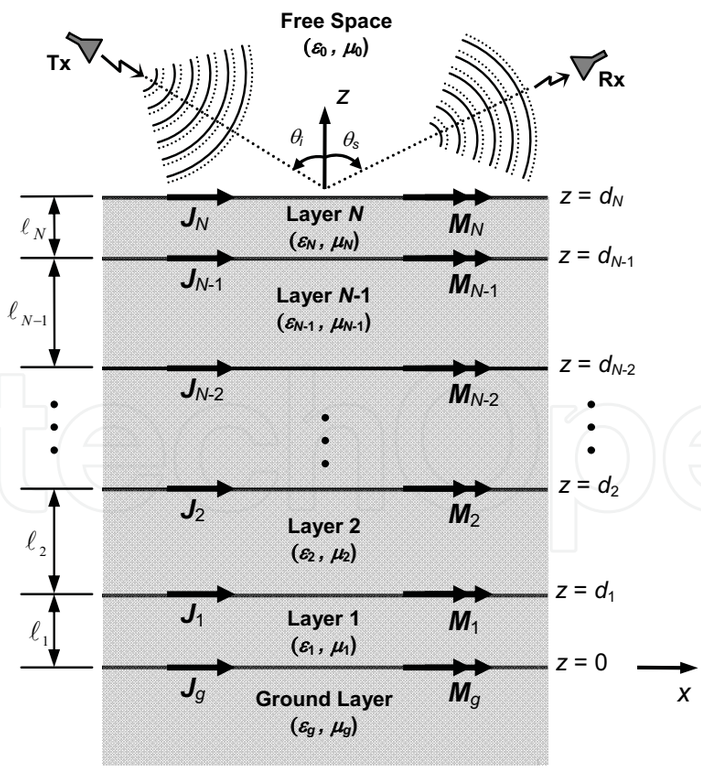

Fig. 1 – Geometry of the planar structure with N+2 layers (lateral view).

This electromagnetic modeling for multilayer structures is completely described in (Sant'Anna, 2009) and it can be synthetically summarized in the flowchart illustrated on Figure 2. In this figure it is shown step by step the entire approach to obtain the far electromagnetic fields scattered by the multilayer structure. Starting from the wave equation in each layer, the methodological flowchart highlights the Green's functions acquirement and the integral equations formulation, which are solved applying the method of moments.

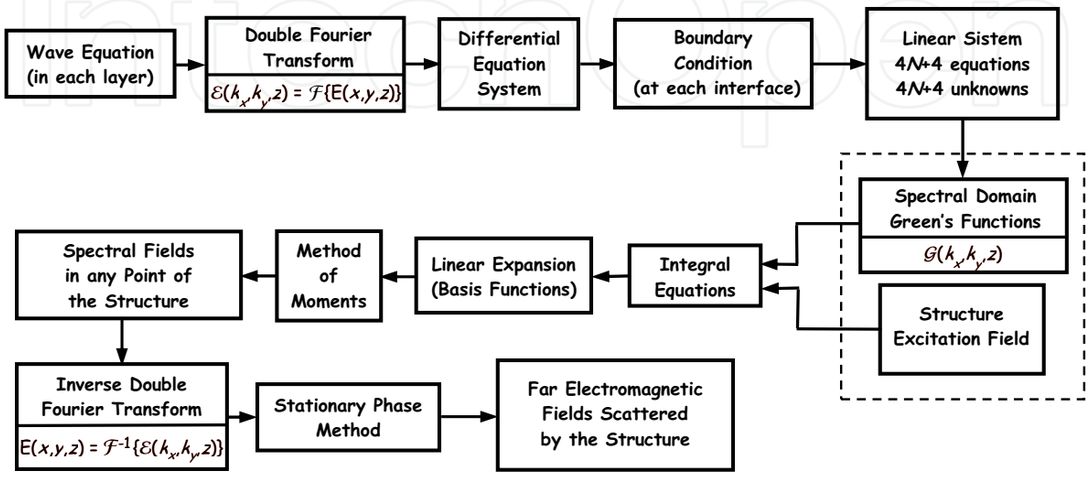

Fig. 2 – Methodological flowchart.

2.1 Electromagnetic Fields in the Structure

The electromagnetic fields in a multilayer structure can be determined through the methodological approach described in (Lacava et al., 2002). According to this methodology, which employs the spectral domain full-wave technique, the structure is treated as a boundary value problem, where the surface current densities induced on the printed elements (electric or magnetic) are the virtual sources of the scattered fields. Since the layers of the structure are free of sources, assuming time dependence of the form $e^{i\omega t}$, the wave equations for the n-th layer is written as

$$\nabla^2 \boldsymbol{E}_n(x,y,z) + k_n^2 \, \boldsymbol{E}_n(x,y,z) = 0 \,, \tag{1}$$

$$\nabla^2 \boldsymbol{H}_n(x,y,z) + k_n^2 \, \boldsymbol{H}_n(x,y,z) = 0 \,, \tag{2}$$

where for free space $n = 0$ and for ground layer $n = g$, $k_n^2 = \omega^2 \mu_n \varepsilon_n$ gives the wave number in the n-th layer, ω is the angular frequency, and the vectors $\boldsymbol{E}_n(x,y,z)$ and $\boldsymbol{H}_n(x,y,z)$ denote the complex electric and magnetic fields, respectively (bold face letters represent vectors). The wave equations can be solved in the spectral domain using the double Fourier transform. In this work, the Fourier transform pair is defined as

$$\boldsymbol{\mathcal{F}}(k_x,k_y,z) = \int_{-\infty}^{+\infty}\int \boldsymbol{F}(x,y,z)\, e^{i(k_x x + k_y y)} \, dx\,dy \,, \tag{3}$$

$$\boldsymbol{F}(x,y,z) = \frac{1}{4\pi^2} \int_{-\infty}^{+\infty}\!\!\int \mathfrak{F}(k_x,k_y,z)\, e^{-i(k_x x + k_y y)}\, dk_x\, dk_y\,, \tag{4}$$

where the function $\boldsymbol{F}(x,y,z)$ represents the fields $\boldsymbol{E}_n(x,y,z)$ and $\boldsymbol{H}_n(x,y,z)$. Applying the double Fourier transform to (1) and (2) yields a differential equation system whose solution, in terms of the field components, is given by

$$\mathcal{E}_{n\tau\vartheta}(k_x,k_y,z) = \mathfrak{e}_{n\tau\vartheta}(k_x,k_y)\, e^{i\gamma_{n\tau}z}\,, \tag{5}$$

$$\mathcal{H}_{n\tau\vartheta}(k_x,k_y,z) = \mathfrak{h}_{n\tau\vartheta}(k_x,k_y)\, e^{i\gamma_{n\tau}z}\,, \tag{6}$$

with

$$\gamma_{n\tau} = (-1)^{\tau}\sqrt{k_n^2 - (k_x^2 + k_y^2)}\,, \quad \mathrm{Im}(\gamma_{n\tau}) \le 0 \tag{7}$$

where $\mathfrak{e}_{n\tau\vartheta}(k_x,k_y)$ and $\mathfrak{h}_{n\tau\vartheta}(k_x,k_y)$ are the amplitudes of the transformed field components, k_x and k_y are the spectral variables, $\gamma_{n\tau}$ is the τ-th propagation constant in the n-th layer, $\vartheta = x$, y or z, and Im( ) means the imaginary-part of a complex function. The variable τ, which defines the wave propagation direction, can assume values 1 or 2. Only the former value, representing propagation in the positive-z direction, occurs in the upper layer (free space). In this case the wave propagation constant will be denoted by γ_0. For the ground layer, on the other hand, τ is equal to 2, i.e., a wave propagating in the negative-z direction and the propagation constant is represented by γ_g. For the inner layers, however, both values of τ will occur, resulting in $\gamma_{n1} = -\gamma_{n2}$ and the wave propagation constant is denoted by γ_n.

Interesting relations among the amplitudes of the transformed fields are derived by introducing the inverse Fourier transform of (5) and (6) in the Maxwell's curl equations. Such that the amplitudes of the transversal components (x and y directions) are written as functions of the amplitude of the longitudinal ones (z direction). By enforcing the boundary conditions for the electromagnetic fields at each interface a set of $4N$+4 equations with equal number of unknowns is obtained. The analytical solution of this system leads to the spectral domain Green's functions. These functions, jointly with the transformed surface current densities, allow the determination of the transformed fields at any point of the multilayer structure. The transformed electromagnetic field components are expressed by

$$\begin{aligned}\mathcal{E}_{n\vartheta}(k_x,k_y,z) = {} & \sum_{\upsilon} \mathcal{G}^{(n)}_{\vartheta\upsilon x}(k_x,k_y,z)\, j_{\upsilon x}(k_x,k_y) + \sum_{\upsilon} \mathcal{G}^{(n)}_{\vartheta\upsilon y}(k_x,k_y,z)\, j_{\upsilon y}(k_x,k_y) + \\ & \sum_{\upsilon} \mathcal{Q}^{(n)}_{\vartheta\upsilon x}(k_x,k_y,z)\, m_{\upsilon x}(k_x,k_y) + \sum_{\upsilon} \mathcal{Q}^{(n)}_{\vartheta\upsilon y}(k_x,k_y,z)\, m_{\upsilon y}(k_x,k_y)\,,\end{aligned} \tag{8}$$

$$\begin{aligned}\mathcal{H}_{n\vartheta}(k_x,k_y,z) = {} & \sum_{\upsilon} \mathcal{P}^{(n)}_{\vartheta\upsilon x}(k_x,k_y,z)\, j_{\upsilon x}(k_x,k_y) + \sum_{\upsilon} \mathcal{P}^{(n)}_{\vartheta\upsilon y}(k_x,k_y,z)\, j_{\upsilon y}(k_x,k_y) + \\ & \sum_{\upsilon} \mathcal{R}^{(n)}_{\vartheta\upsilon x}(k_x,k_y,z)\, m_{\upsilon x}(k_x,k_y) + \sum_{\upsilon} \mathcal{R}^{(n)}_{\vartheta\upsilon y}(k_x,k_y,z)\, m_{\upsilon y}(k_x,k_y)\,,\end{aligned} \tag{9}$$

where $G^{(n)}_{\vartheta\upsilon\varsigma}(k_x,k_y,z)$ and $Q^{(n)}_{\vartheta\upsilon\varsigma}(k_x,k_y,z)$ represent, respectively, the spectral domain Green's functions of electric type in the n-th layer, which relate the ς ($\varsigma = x$ or y) components of the electric field to the transformed surface current densities $j_{\iota\varsigma}(k_x, k_y)$ and $m_{\iota\varsigma}(k_x, k_y)$ located at the interface d_ι, with $\upsilon \in \{g, 1, 2, \ldots, N\}$, and $P^{(n)}_{\vartheta\upsilon\varsigma}(k_x,k_y,z)$ and $R^{(n)}_{\vartheta\upsilon\varsigma}(k_x,k_y,z)$ are the respective spectral domain Green's functions of magnetic type. Note that $d_g = 0$ for the structure defined in Figure 1.

In order to demonstrate the mathematical aspect of the spectral domain Green's functions, it is shown in equations (10) and (11) examples of electric and magnetic function types, respectively, for free-space region. These equations are obtained when the structure is composed by four layers ($N = 2$).

$$G^{(0)}_{x2x}(k_x,k_y,z) = -\frac{4\omega^2}{(k_x^2+k_y^2)}\left\{\frac{k_x^2\gamma_0\Theta_2}{\Delta_1}+\frac{k_y^2\omega\mu_0\Xi_2}{\Delta_2}\right\}e^{-i\gamma_0 z}, \tag{10}$$

$$R^{(0)}_{x2x}(k_x,k_y,z) = -\frac{4\omega^2}{(k_x^2+k_y^2)}\left\{\frac{k_y^2\omega\varepsilon_0\Theta_5}{\Delta_1}+\frac{k_x^2\gamma_0\Xi_5}{\Delta_2}+\right\}e^{-i\gamma_0 z}, \tag{11}$$

where

$$\Delta_1 = -4\omega^3 e^{-i\alpha_0}\{\varepsilon_1\gamma_2(\varepsilon_2\gamma_0\cos\alpha_2+i\varepsilon_0\gamma_2\sin\alpha_2)(\varepsilon_g\gamma_1\cos\alpha_1+i\varepsilon_1\gamma_g\sin\alpha_1)+ \varepsilon_2\gamma_1(\varepsilon_0\gamma_2\cos\alpha_2+i\varepsilon_2\gamma_0\sin\alpha_2)(\varepsilon_1\gamma_g\cos\alpha_1+i\varepsilon_g\gamma_1\sin\alpha_1)\}, \tag{12}$$

$$\Delta_2 = 4\omega^3 e^{-i\alpha_0}\{\mu_1\gamma_2(\mu_2\gamma_0\cos\alpha_2+i\mu_0\gamma_2\sin\alpha_2)(\mu_g\gamma_1\cos\alpha_1+i\mu_1\gamma_g\sin\alpha_1)+ \mu_2\gamma_1(\mu_0\gamma_2\cos\alpha_2+i\mu_2\gamma_0\sin\alpha_2)(\mu_1\gamma_g\cos\alpha_1+i\mu_g\gamma_1\sin\alpha_1)\}, \tag{13}$$

$$\Theta_2 = \gamma_2\{\varepsilon_1\gamma_2(\varepsilon_1\gamma_g\sin\alpha_1 - i\varepsilon_g\gamma_1\cos\alpha_1)\sin\alpha_2 - \varepsilon_2\gamma_1(\varepsilon_1\gamma_g\cos\alpha_1+i\varepsilon_g\gamma_1\sin\alpha_1)\cos\alpha_2\}, \tag{14}$$

$$\Theta_5 = -\omega\varepsilon_2\{\varepsilon_1\gamma_2(\varepsilon_g\gamma_1\cos\alpha_1+i\varepsilon_1\gamma_g\sin\alpha_1)\cos\alpha_2 - \varepsilon_2\gamma_1(\varepsilon_g\gamma_1\sin\alpha_1 - i\varepsilon_1\gamma_g\cos\alpha_1+)\sin\alpha_2\}, \tag{15}$$

$$\Xi_2 = \omega\mu_2\{\mu_1\gamma_2(\mu_g\gamma_1\cos\alpha_1+i\mu_1\gamma_g\sin\alpha_1)\cos\alpha_2 - \mu_2\gamma_1(\mu_g\gamma_1\sin\alpha_1 - i\mu_1\gamma_g\cos\alpha_1)\sin\alpha_2\}, \tag{16}$$

$$\Xi_5 = \gamma_2\{\mu_2\gamma_1(\mu_1\gamma_g\cos\alpha_1+i\mu_g\gamma_1\sin\alpha_1)\cos\alpha_2 - \mu_1\gamma_2(\mu_1\gamma_g\sin\alpha_1 - i\mu_g\gamma_1\cos\alpha_1)\sin\alpha_2\}, \tag{17}$$

with $\alpha_0 = \gamma_0 d_2$, $\alpha_1 = \gamma_1 d_1$, $\alpha_2 = \gamma_2 (d_2 - d_1)$, $d_1 = \ell_1$ and $d_2 = \ell_1 + \ell_2$. It can be noted that the Green's functions carry information of electromagnetic parameters from all structure layers.

2.2 Method of Moments (MoM)

Once the Green's functions are derived, the next step is to set up integral equations constrained to the required boundary conditions. The integral equations arise as a combination of the Green's functions and the structure excitation fields, as can be seen from the dashed box in Figure 2. The boundary conditions are related to the total electric and magnetic tangential

fields to each respective scattering element. The subsequent development will be described only when electric elements are present in the structure. However, it could be also applied to magnetic elements, taking into account its specific nature. Therefore, the integral equation is a statement of the boundary condition requiring that the total electric field tangential to the each of the electric element is zero (Newman & Forrai, 1987). That is,

$$\boldsymbol{z}\times[\boldsymbol{E}^{i}(x,y,d_{\upsilon})+\boldsymbol{E}^{r}(x,y,d_{\upsilon})]=-\boldsymbol{z}\times\boldsymbol{E}^{s}(x,y,d_{\upsilon})\text{, on } S_{\upsilon} \tag{18}$$

where S_υ is the support region of the electric element, $\boldsymbol{E}^s(x,y,d_\upsilon)$ denotes the scattered electric field excited by the current on S_υ, $\boldsymbol{E}^i(x,y,d_\upsilon)$ stands for the incident electric field and $\boldsymbol{E}^r(x,y,d_\upsilon)$ identifies the field that are reflected by the multilayer structure in the absence of electric elements. The incident and reflected fields define the excitation mechanism of the structure, which in this analysis is due to an elliptically polarized plane wave at an arbitrary incidence angle.

The currents induced on the electric elements by these fields are unknown. To solve the integral equations (18), with the unknown surface currents, the method of moments (MoM) is applied. This method is one the most popular numerical techniques used to analyze the radiation and scattering from complex structures. In the MoM, first the surface current is linearly expanded in a set of basis functions with unknown coefficients

$$\boldsymbol{j}_{\upsilon}(k_x,k_y)=\boldsymbol{x}\sum_{m=1}^{M_{L\upsilon}}\sum_{n=1}^{N_{L\upsilon}}I^{x}_{m\upsilon n\upsilon}\,j_{m\upsilon}(k_x,k_y)+\boldsymbol{y}\sum_{m=1}^{M_{L\upsilon}}\sum_{n=1}^{N_{L\upsilon}}I^{y}_{m\upsilon n\upsilon}\,j_{n\upsilon}(k_x,k_y)\text{,} \tag{19}$$

where ML and NL control the expansion modes in x and y directions on each interface layer, respectively, $I^{\varsigma}_{m\upsilon n\upsilon}$ are the complex coefficients in the ς direction ($\varsigma = x$ or y) that need to be determined, and $j_{m\upsilon}(k_x,k_y)$ and $j_{n\upsilon}(k_x,k_y)$ are the Fourier transform of the surface current density components, which are defined only over the electric element. Applying the Galerkin technique (whereby the test functions are chosen to be identical to the basis ones) the integral equation is reduced to a system of simultaneous linear equations, which can be compactly written in matrix form as $[V] = [Z][I]$. In this notation $[V]$, $[Z]$ and $[I]$ denote, respectively, the excitation matrix, the impedance matrix and the coefficient matrix. For example, the integral equation referring to the scattered fields at the interface $z = d_\upsilon$ can be written as

$$\begin{aligned}4\pi^2\iint_{S_\upsilon}E^{s}_{0x}(x,y,d_\upsilon)\,J^{*}_{pn}(x,y)\,dx\,dy=&\sum_{\upsilon=0}^{N}\sum_{m=1}^{M_{L\upsilon}}\sum_{n=1}^{N_{L\upsilon}}I^{x}_{m\upsilon n\upsilon}\int_{-\infty}^{+\infty}\int_{-\infty}^{+\infty}\mathcal{G}^{(0)}_{x\upsilon x}\,j_{m\upsilon}\,j^{*}_{pn}\,dk_x\,dk_y+\\&\sum_{\upsilon=0}^{N}\sum_{m=1}^{M_{L\upsilon}}\sum_{n=1}^{N_{L\upsilon}}I^{y}_{m\upsilon n\upsilon}\int_{-\infty}^{+\infty}\int_{-\infty}^{+\infty}\mathcal{G}^{(0)}_{x\upsilon y}\,j_{n\upsilon}\,j^{*}_{pn}\,dk_x\,dk_y\text{,}\end{aligned} \tag{20}$$

$$4\pi^2\iint_{S_\upsilon}E^{s}_{0y}(x,y,d_\upsilon)\,J^{*}_{qn}(x,y)\,dx\,dy=\sum_{\upsilon=0}^{N}\sum_{m=1}^{M_{L\upsilon}}\sum_{n=1}^{N_{L\upsilon}}I^{x}_{m\upsilon n\upsilon}\int_{-\infty}^{+\infty}\int_{-\infty}^{+\infty}\mathcal{G}^{(0)}_{y\upsilon x}\,j_{m\upsilon}\,j^{*}_{qn}\,dk_x\,dk_y+$$

$$\sum_{\upsilon=0}^{N}\sum_{m=1}^{M_{L\upsilon}}\sum_{n=1}^{N_{L\upsilon}} I^{y}_{m\upsilon n\upsilon}\int_{-\infty}^{+\infty}\int_{-\infty}^{+\infty}\mathcal{G}^{(0)}_{y\upsilon y}\; j_{n\upsilon}\; j^{*}_{qn}\; dk_x\; dk_y\;, \qquad (21)$$

where the left side of (20) and (21) defines the [*V*] matrix, the double integrals are related to the [*Z*] matrix and the variables *p* and *q* range equally to the variables *m* and *n*, respectively. It is important to point out that for notation simplicity the functions $\mathcal{G}^{(0)}_{\vartheta\upsilon\varsigma}(k_x, k_y, d_n)$, $j_{m\upsilon}(k_x, k_y)$ and $j^{*}_{pn}(k_x, k_y)$ were written without their respective variables in equations (20) and (21).

As abovementioned, following the same procedure it is possible to get similar expressions when magnetic elements are used. Nevertheless, the scattered electric field, the transformed surface electric current density and the Green´s function $\mathcal{G}^{(0)}_{\vartheta\upsilon\varsigma}$ should be changed by the scattered magnetic field, the transformed surface magnetic current density and the Green´s function $\mathcal{R}^{(0)}_{\vartheta\upsilon\varsigma}$, respectively.

The double integrations in equation (20) and (21) must be performed numerically, usually in a very inefficient and time-consuming way. In order to improve the computation efficiency some mathematical simplifications are employed. These simplifications include the evaluation of the even and the odd properties of the Green's functions, the change of the coordinate system (rectangular to polar: $k_x = \beta\cos\alpha$ and $k_y = \beta\sin\alpha$) and the asymptotic extraction technique.

2.3 Asymptotic Expressions

In microwave remote sensing applications the major interest consist on the target radiated power and it's carried information. Therefore, is necessary the determination of the far electromagnetic fields scattered by the target. These fields scattered by the multilayer structure are computed based on asymptotic expressions, which are derived from the stationary phase method (Collin & Zucker, 1969). The electric far-field, using this method, is given by

$$\boldsymbol{E}_0(r,\theta,\phi) \cong -\frac{i\,k_0}{2\pi}\frac{e^{-ik_0 r}}{r}\cot\theta\,\left\{\hat{\theta}\,\mathfrak{e}_{0z}(k_{xe},k_{ye}) - \hat{\phi}\,\eta_0\mathfrak{h}_{0z}(k_{xe},k_{ye})\right\}, \qquad (22)$$

in a spherical coordinate system, where the intrinsic impedance of free space is represented by η_0, $k_{xe} = k_0\sin\theta\cos\phi$ and $k_{ye} = k_0\sin\theta\sin\phi$ are the stationary phase points, k_0 is the wave number of the excitation wave, $\mathfrak{e}_{0z}(k_{xe}, k_{ye})$ and $\mathfrak{h}_{0z}(k_{xe}, k_{ye})$ are the amplitudes of the transformed far-field components (in the *z* direction) in free space and *r* characterizes the distance between the receiving antenna and the target. Note that the far magnetic field $\boldsymbol{H}_0(r, \theta, \phi)$ might be obtained from $\boldsymbol{E}_0(r, \theta, \phi)$. For instance, considering a particular structure consisting of four layers ($N = 2$) and having electric and magnetic elements printed on each interface, the $\mathfrak{e}_{0z}(k_{xe}, k_{ye})$ and $\mathfrak{h}_{0z}(k_{xe}, k_{ye})$ are expressed by

$$\mathfrak{e}_{0z}(k_{xe},k_{ye}) = \frac{4\omega^2}{\Delta_1}\Big\{(k_{xe}\Theta_0)j_{gx} + (k_{ye}\Theta_0)j_{gy} + (k_{xe}\Theta_1)j_{1x} + (k_{ye}\Theta_1)j_{1y} + (k_{xe}\Theta_2)j_{2x} + (k_{ye}\Theta_2)j_{2y} + (k_{ye}\Theta_3)m_{gx} + (-k_{xe}\Theta_3)m_{gy} + (k_{ye}\Theta_4)m_{1x} + (-k_{xe}\Theta_4)m_{1y} + (-k_{ye}\Theta_5)m_{2x} + (k_{xe}\Theta_5)m_{2y}\Big\}, \quad (23)$$

$$\mathfrak{h}_{0z}(k_{xe},k_{ye}) = \frac{4\omega^2}{\Delta_2}\Big\{(-k_{ye}\Xi_0)j_{gx} + (k_{xe}\Xi_0)j_{gy} + (-k_{ye}\Xi_1)j_{1x} + (k_{xe}\Xi_1)j_{1y} + (k_{ye}\Xi_2)j_{2x} + (-k_{xe}\Xi_2)j_{2y} + (k_{xe}\Xi_3)m_{gx} + (k_{ye}\Xi_3)m_{gy} + (k_{xe}\Xi_4)m_{1x} + (k_{ye}\Xi_4)m_{1y} + (k_{xe}\Xi_5)m_{2x} + (k_{ye}\Xi_5)m_{2y}\Big\}, \quad (24)$$

with

$$\Theta_0 = -\varepsilon_1\varepsilon_2\gamma_1\gamma_2\gamma_g, \quad (25)$$

$$\Theta_1 = -\varepsilon_2\gamma_1\gamma_2(\varepsilon_1\gamma_g\cos\alpha_1 + i\varepsilon_g\gamma_1\sin\alpha_1), \quad (26)$$

$$\Theta_3 = \omega\varepsilon_1\varepsilon_2\varepsilon_g\gamma_1\gamma_2, \quad (27)$$

$$\Theta_4 = \omega\varepsilon_1\varepsilon_2\gamma_2(\varepsilon_g\gamma_1\cos\alpha_1 + i\varepsilon_1\gamma_g\sin\alpha_1), \quad (28)$$

$$\Xi_0 = -\omega\mu_1\mu_2\mu_g\gamma_1\gamma_2, \quad (29)$$

$$\Xi_1 = -\omega\mu_1\,\mu_2\gamma_2(\mu_g\gamma_1\cos\alpha_1 + i\mu_1\gamma_g\sin\alpha_1), \quad (30)$$

$$\Xi_3 = \mu_1\mu_2\gamma_1\gamma_2\gamma_g, \quad (31)$$

$$\Xi_4 = \mu_2\gamma_1\,\gamma_2(\mu_1\gamma_g\cos\alpha_1 + i\mu_g\gamma_1\sin\alpha_1), \quad (32)$$

where the terms Δ_1, Δ_2, Θ_2, Θ_5, Ξ_2 and Ξ_5 are given, respectively, by equations (12) to (17). It is important to observe that all terms of equations (23) and (24) are obtained on stationary phase points and the transformed surface current densities were written without their respective variables.

2.4 Simple Target

In order to complete the electromagnetic modeling development, simple target embedded in a multilayer structure consisting of four layers is considered. The simple targets are represented by electric and magnetic rectangular dipoles having infinitesimal thickness, oriented along the x direction and printed on interface $z = d_2$. The dipoles size $2a$ and $2b$ ($a >> b$) in the x and the y directions, respectively. In this particular situation, the surface current density along the y direction is neglected since the dipoles width is considered to be very thin. Thus, for either dipole only the $\left[Z_{p2m2}^{x2x2}\right]$ matrix needs to be evaluated, being represented by $[Z_{pm\zeta}]$, where the variable ζ defines the type of dipole, electric (ζ = **e**) or magnetic (ζ = ***m***). This evaluation involves the Green's functions $\mathcal{G}_{x2x}^{(0)}$ (electric dipole) or $\mathcal{R}_{x2x}^{(0)}$ (magnetic dipole). After the aforementioned mathematical simplifications (subsection 2.2), the $[Z_{pm\zeta}]$ matrix becomes

$$\left[Z_{pm\zeta}\right] = -\frac{1}{4\pi^2}\int_{-\infty}^{+\infty}\int_{-\infty}^{+\infty}\mathcal{A}_{x2x}^{(0)}(k_x,k_y,d_2)\,\mathcal{J}_{m2}(k_x,k_y)\,\mathcal{J}_{p2}^{*}(k_x,k_y)\,dk_x\,dk_y =$$

$$= \frac{1}{\pi^2}\left\{\int_{\beta=0}^{+\infty}\int_{\alpha=0}^{\pi/2}[A_{1\zeta}(\cos\alpha)^2 + A_{2\zeta}(\sin\alpha)^2]\,\mathcal{R}_{pm\,\zeta}\,d\alpha\,d\beta + \right.$$

$$\left.\int_{\beta=0}^{+\infty}\int_{\alpha=0}^{\pi/2}\frac{i\,A_{3\zeta}}{\omega}(\cos\alpha)^2\,\mathcal{R}_{pm\,\zeta}\,d\alpha\,d\beta\right\}, \tag{34}$$

where $\mathcal{A}_{x2x}^{(0)}$ represents the spectral Green's function and $\mathcal{J}_{m2}$ means the transformed surface current density. The spectral Green's function will be defined by $\mathcal{G}_{x2x}^{(0)}$ or by $\mathcal{R}_{x2x}^{(0)}$ in the electric and magnetic dipole cases, respectively. Similarly, the transformed surface current density will be described by j_{m2} or m_{m2}. In each dipole case, the factors $A_{1\zeta}$, $A_{2\zeta}$, $A_{3\zeta}$ and $\mathcal{R}_{pm\zeta}$ are expressed by

$$A_{1\mathbf{e}} = \frac{4\omega^2\beta\gamma_0\Theta_2}{\Delta_1} - \frac{i\,A_{3\mathbf{e}}}{\omega}, \tag{35}$$

$$A_{2\mathbf{e}} = \frac{4\omega^3\beta\mu_0\Xi_2}{\Delta_2}, \tag{36}$$

$$A_{3\mathbf{e}} = \frac{\beta^2}{\varepsilon_0+\varepsilon_2}, \tag{37}$$

$$A_{1\mathbf{m}} = \frac{1}{\omega}\left(\frac{\beta\gamma_0\Xi_5}{\Delta_2} - i\,A_{3\mathbf{m}}\right), \tag{38}$$

$$A_{2\mathbf{m}} = \frac{\beta\varepsilon_0\Theta_5}{\Delta_1}, \tag{39}$$

$$A_{3\mathbf{m}} = \frac{\beta^2}{\mu_0+\mu_2}, \tag{40}$$

$$\mathcal{R}_{pm\,\mathbf{e}} = \pi^2 b^2 J_0^2(bk_y)\,\mathrm{sinc}^4(k_x\Delta x/2)\cos[k_x(x_m - x_p)], \tag{41}$$

with $\mathcal{R}_{pm\mathbf{m}} = \mathcal{R}_{pm\mathbf{e}}$.

Additionally the equation (41) is obtained from the modeling of the surface electric current density as the summation of piecewise-linear subdomain basis functions (rooftop functions) taking into account the edge condition. In this equation sinc(χ) = sin(χ)/χ, $J_0(.)$ stands for the zero-order Bessel function of the first kind and $\Delta x = 2a/(M+1)$, where M is the number of current expansion modes.

From (34) to (41) it is noted that the first double integral of $[Z_{pm\zeta}]$ is dependent on the operating frequency, whereas the second one is not. The former is the well-known Sommerfeld integrals, which exhibit singularities in the form of branch points and poles; as such, their computation requires careful attention. The poles (generally complex) correspond to surface and leaky waves that can be excited in the layers. According to (Marin et al., 1990) the number of surface

wave poles and their locations depends on the thickness of the layers, their electromagnetic parameters and the wave number. For a multilayer structure and depending on the thickness of the layers, the Green's functions might present hundreds of poles, making their integration a formidable task. Since the number of poles and their locations are not known beforehand (Newman & Forrai, 1987), the use of a deformed path to compute the integrations seems to be an efficient way to avoid this problem. Therefore, in this work a parabolic path was chosen to compute the integrations.

Using the rooftop function as basis function, the excitation matrices $[V_{p\mathbf{e}}]$ and $[V_{p\mathbf{m}}]$, for this particular structure, are defined only over the S_2 region, which is limited by $-a$ and $+a$ in x-direction and by $-b$ and $+b$ in y-direction being given by

$$\left[V_{p\zeta}\right] = \iint_{S_2} F(x,y,d_2)\,\mathcal{D}^*_{p2x}(x)\,\mathcal{D}^*_{p2y}(y)\,dx\,dy = \\ = 2\,(B_\zeta \sin\varphi_i + C_\zeta \cos\varphi_i)\,\mathrm{sinc}^2(\Psi_1 \Delta x/2)\; e^{i\Psi_1 x_p} \int_0^{+b} \frac{\cos(\Psi_2 y)}{\sqrt{1-(y/b)^2}}\,dy\,, \quad (42)$$

where variable ζ (e or m) defines the type of dipole as defined in equation (34). Therefore, the function $F(x, y, d_2)$ can represent the scattered field $E^s_{0x}(x,y,d_2)$ or $H^s_{0x}(x,y,d_2)$ and the complex conjugate of the surface current density $\mathcal{D}^*_{p2\varsigma}$ will stand for $J^*_{p2\varsigma}$ or $M^*_{p2\varsigma}$, with $\varsigma = x$ or y. The constants B_ζ, C_ζ, Ψ_1 and Ψ_2 are given by

$$B_{\mathbf{e}} = -(E^i_h e^{i\Omega} + E^r_h e^{-i\Omega})\,, \quad (43)$$

$$C_{\mathbf{e}} = -\cos\theta_i\,(E^i_v e^{i\Omega} - E^r_v e^{-i\Omega})\,, \quad (44)$$

$$B_{\mathbf{m}} = -\eta_0^{-1}\,(E^i_v e^{i\Omega} + E^r_v e^{-i\Omega})\,, \quad (45)$$

$$C_{\mathbf{m}} = -\eta_0^{-1}\cos\theta_i\,(-E^i_h e^{i\Omega} + E^r_h e^{-i\Omega})\,, \quad (46)$$

$$\Psi_1 = k_0 \sin\theta_i \cos\phi_i\,, \quad (47)$$

$$\Psi_2 = k_0 \sin\theta_i \sin\phi_i\,, \quad (48)$$

with $\Omega = k_0\, d_2 \cos\theta_i$, E^i_p and E^r_p standing for incident and reflected electric fields having linear p polarization (horizontal or vertical) and the angles θ_i and ϕ_i define the direction of the incident wave. In equations (43) to (48) the subscript v and h stand for vertical and horizontal linear polarization. The solution of integral equation leads to coefficient matrix $[I]$, from which it is possible to obtain the surface current density expression over the scattering element. This density jointly with the spectral Green's function permits the evaluation of the electromagnetic fields in spectral domain.

3. Remote Sensing Applications

This section is devoted to some remote sensing applications, which can be derived from the electromagnetic modeling described in section 2. All results are referred to a simple target (electric and/or magnetic dipoles) embedded in a four layers structure ($N = 2$).

3.1 Scattering Matrix

The determination of analytical expressions for the dipoles scattering matrices is the first application considered in this section. The scattering matrix is the most important parameter in polarimetric SAR analysis, since it provides complete information about the scattering mechanism. All polarimetric features that describe the target scattering can be derived from it. The scattering matrix can be seen as a mathematical characterization of the target scattering. This matrix linearly relates the electric fields of the wave scattered ($\boldsymbol{E}^s$) by a target to the ones of the incident wave ($\boldsymbol{E}^i$). As consequence the scattering matrix can be seen as a linear operator between $\boldsymbol{E}^s$ and $\boldsymbol{E}^i$, given by

$$\left[\boldsymbol{E}^s\right]=\begin{bmatrix}E_v^s\\E_h^s\end{bmatrix}=\frac{e^{-ik_0r}}{r}\begin{bmatrix}S_{vv} & S_{vh}\\S_{hv} & S_{hh}\end{bmatrix}\begin{bmatrix}E_v^i\\E_h^i\end{bmatrix}=\frac{e^{-ik_0r}}{r}[S]\left[\boldsymbol{E}^i\right], \tag{49}$$

where the subscript v and h stand for vertical and horizontal linear polarization. In order to determine the scattering matrix of electric and magnetic dipoles embedded in a multilayer structure, as illustrated in Figure 3, the procedure defined in (Sant'Anna et al., 2007a) will be followed. This procedure directly relates the elements of the scattering matrix to the components of the scattered electric field; a standard spherical coordinate system (r, θ, ϕ) is chosen to coincide with a coordinate system (k, v, h) defined in terms of horizontal and vertical linear polarization components, as stated in (Ulaby & Elachi, 1990).

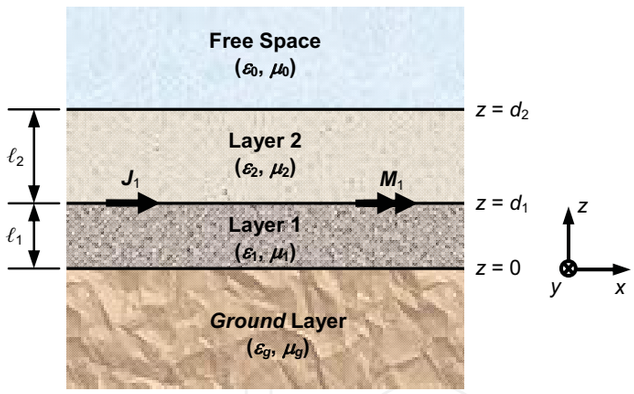

Fig. 3 – A lateral view of the multilayer structure under analysis.

The incident wave sets up currents on the scattering elements (dipoles), which in turn re-radiates a scattered wave. The currents induced on the dipoles depend on the incident wave polarization. Therefore, from the reciprocity theorem, relation (50) between the components of the transformed far electric field in free space due to each linear polarization

$$\mathfrak{e}_{0z}^{(h)}(k_{xe},k_{ye})=-\eta_0\mathfrak{h}_{0z}^{(v)}(k_{xe},k_{ye}), \tag{50}$$

can be obtained, where the superscripts (v, h) are associated to polarization of the incident wave. Consequently, for an electric planar dipole the induced currents due to horizontal and vertical linear polarizations are, then, related by

$$j_{1xe}^{(h)}(k_{xe},k_{ye})=-\mathbb{C}_1\left(\frac{k_{ye}}{k_{xe}}\right)j_{1xe}^{(v)}(k_{xe},k_{ye}). \tag{51}$$

This relation leads to the following scattering matrix

$$[S_{ed}] = \frac{\mathbb{C}_2}{\cos\phi_s}\begin{bmatrix} (\cos\phi_s)^2/\mathbb{C}_1 & \sin\phi_s\cos\phi_s \\ \sin\phi_s\cos\phi_s & \mathbb{C}_1(\sin\phi_s)^2 \end{bmatrix}, \tag{52}$$

where the constants $\mathbb{C}_1$ and $\mathbb{C}_2$ are given by

$$\mathbb{C}_1 = \frac{\Delta_1\Xi_1}{\Delta_2\Theta_1}\eta_0 \text{ and } \quad \mathbb{C}_2 = -\frac{i2\omega^2 k_0^2\eta_0\Xi_1}{\pi\Delta_2}\cos\theta_s\, j_{1xe}^{(v)}(k_{xe},k_{ye}).$$

Similarly for the magnetic dipole, the relation between the induced currents and its corresponding scattering matrix are expressed, respectively, by

$$m_{1xe}^{(h)}(k_{xe},k_{ye}) = -\mathbb{C}_3\left(\frac{k_{xe}}{k_{ye}}\right)m_{1xe}^{(v)}(k_{xe},k_{ye}), \tag{53}$$

$$[S_{md}] = \frac{\mathbb{C}_4}{\sin\phi_s}\begin{bmatrix} (\sin\phi_s)^2/\mathbb{C}_3 & -\sin\phi_s\cos\phi_s \\ -\sin\phi_s\cos\phi_s & \mathbb{C}_3(\cos\phi_s)^2 \end{bmatrix}, \tag{54}$$

where the constants $\mathbb{C}_3$ and $\mathbb{C}_4$ are represented by

$$\mathbb{C}_3 = \frac{\Delta_1\Xi_4}{\Delta_2\Theta_4}\eta_0 \text{ and } \quad \mathbb{C}_4 = -\frac{i2\omega^2 k_0^2\eta_0\Xi_4}{\pi\Delta_2}\cos\theta_s\, m_{1xe}^{(v)}(k_{xe},k_{ye}).$$

Note that the constants $\mathbb{C}_2$ and $\mathbb{C}_4$, which are directly related to the currents induced on the dipoles, affect equally all the elements of the scattering matrices. The terms Δ_1, Δ_2, Θ_1, Θ_4, Ξ_1 and Ξ_4, given by equations (12), (13), (26), (28), (30) and (32) respectively, are evaluated at stationary phase points. From equations (52) and (54) it can be also observed that the scattering matrix expressions are derived for any direction of the scattered wave.

In (Sant'Anna et al., 2008a) it was used two polarimetric features as comparative metrics between the electric and magnetic scattering matrices. These features included the α-angle derived from the eigenvalue/eigenvector decomposition (Cloude & Pottier, 1997) and a similarity measurement based on square of correlation coefficient, which was proposed in (Yang et al., 2001). The results were obtained in (Sant'Anna et al., 2008a) for a structure composed of layers having the same electromagnetic parameters of free space. They showed that even though the dipoles present different electromagnetic nature the dominant α-angle for both are equal to 45°. Therefore, based on this feature it was not possible to differentiate the two dipoles, despite their electromagnetic characteristics. On the other hand, measuring the correlation coefficient it was shown that it can be used as a discriminating feature between the two scattering matrices. This statement is promptly verified when the four layers are assumed to be the free space. In this particular case the constants $\mathbb{C}_1$ and $\mathbb{C}_3$ are reciprocal real values yielding a correlation coefficient equal to zero, i.e. the scattering matrices are non-similar.

3.2 Simple Target Characterization

The simple target characterization is the second application considered in this work within remote sensing context. The characterization is made using several electromagnetic attributes that are measured at far-field condition. The measurements are done based on a particular configuration of the four layers structure, in which the dielectric parameters of layers 1 and 2 are made equals. That is, the structure is then composed by three dielectric layers (the free-space region, one inner layer and the ground layer) and the dipoles (electric and magnetic) are printed on interface $z = d_2$, as depicted in Figure 4.

In antenna theory the directivity function $\mathbb{D}(\theta, \phi)$ is one of several parameters used to characterize or define an antenna. According to (Balanis, 1997) this function is defined as the ratio of the radiation intensity $\mathbb{U}(\theta, \phi)$ in a given direction from the antenna to the radiated intensity average over all direction. The $\mathbb{D}(\theta, \phi)$ is expressed by

$$\mathbb{D}(\theta,\phi) = \frac{4\,\pi\,\mathbb{U}(\theta,\phi)}{\mathbb{P}_i}\,, \tag{55}$$

where $\mathbb{P}_i = \int_{\Omega} \mathbb{U}(\theta,\phi)\, d\Omega$ is the average radiated power within the solid angle Ω and the $\mathbb{U}(\theta, \phi)$ function is defined, for a multilayer structure, as

$$\mathbb{U}(\theta,\phi) = \frac{1}{2\eta_0}\left(\frac{k_0 \cot\theta}{2\,\pi}\right)^2 \left\{ \left| \mathfrak{e}_{0z}(k_{xe}, k_{ye}) \right|^2 + \eta_0^2 \left| \mathfrak{h}_{0z}(k_{xe}, k_{ye}) \right|^2 \right\}, \tag{56}$$

with the transformed electric and magnetic longitudinal amplitudes the $\mathfrak{e}_{0z}(k_{xe}, k_{ye})$ and $\mathfrak{h}_{0z}(k_{xe}, k_{ye})$ being expressed by equations (23) and (24), respectively.

Considering the structure of Figure 4 and assuming that the size of dipoles are infinitesimal the function $\mathbb{D}(\theta, \phi)$ is promptly computed. Since, in this case, the surface current density can be considered as constant. The directivity function for a structure characterized by $\varepsilon_r = 2$, $\mathrm{tg}\delta = 0$, $\varepsilon_{rg} = 1$ and $\mathrm{tg}\delta_g = 1.0\times10^{+15}$ as dielectric parameters values, it was evaluated at 2.25 GHz for printed infinitesimal electric and magnetic dipoles. The respective three-dimensional graphic of $\mathbb{D}(\theta, \phi)$ are illustrated in Figures 5 and 6 for two values of inner layer thickness, $\ell = 4$ mm ($0.03\lambda_0$) and $\ell = 40$ mm ($0.3\lambda_0$).

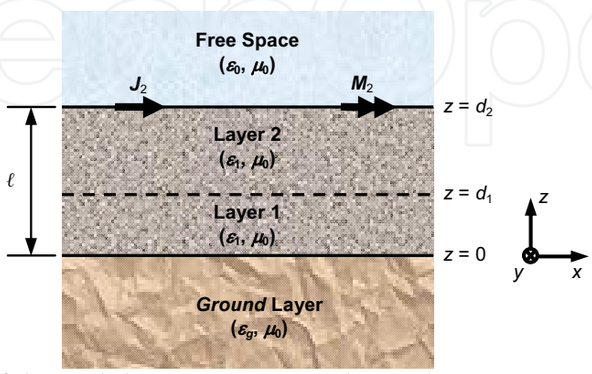

Fig. 4 – A lateral view of the multilayer structure under analysis.

From these figures it can be notice that the radiation patterns are completely different for both dipoles. This fact it was expected due to the dissimilar electromagnetic feature of the dipoles. Theoretically, the radiation pattern can be used to differentiate structures which present these kinds of dipoles. In addition, it can be observed that the shapes as well as the radiation levels are modified by the variation of the inner layer thickness. The radiation levels modification may be associated to the modes (guided and leaky) existing within the structure. Increasing the layer thickness more guided modes might be established inside the structure, consequently decreasing its scattered power.

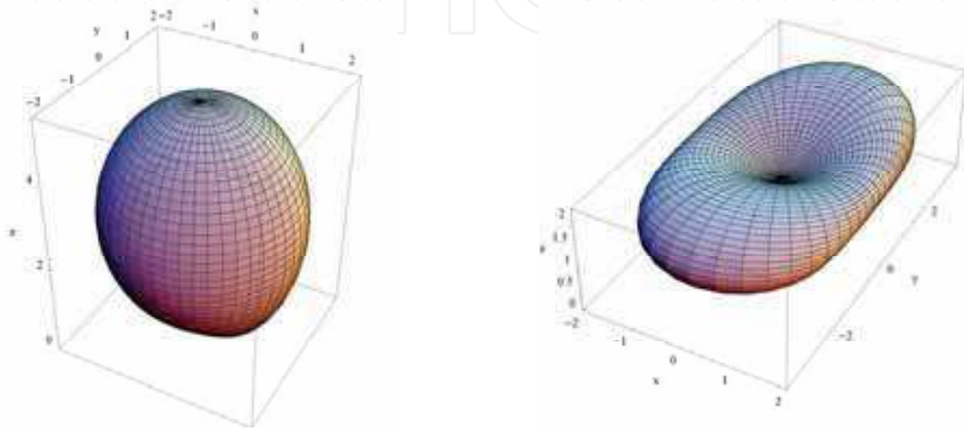

(a) (b)

Fig. 5 – Three-dimensional graphic of $\mathbb{D}(\theta, \phi)$ for infinitesimal electric dipole: (a) ℓ = 4 mm and (b) ℓ = 40 mm.

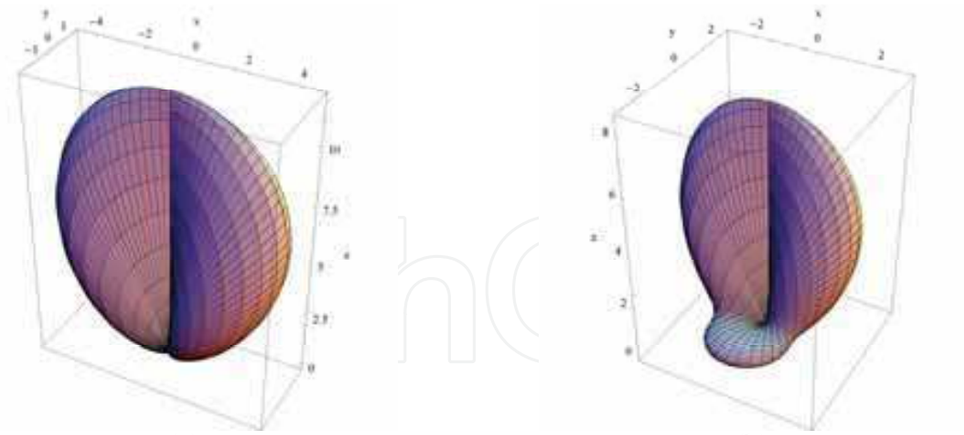

(a) (b)

Fig. 6 – Three-dimensional graphic of $\mathbb{D}(\theta, \phi)$ for infinitesimal magnetic dipole: (a) ℓ = 4 mm and (b) ℓ = 40 mm.

The *SCS* is other parameter that can be used on the characterization of target scattering properties. In general, it is function of the operating frequency, wave polarization, incident and observation angles, target geometry and its dielectric properties. According to (IEEE, 1993) the target *SCS* can be expressed by

$$SCS(\boldsymbol{k}_s, \boldsymbol{k}_i) = \lim_{r\to\infty}\left[4\pi r^2 \frac{\left|\boldsymbol{E}^s(\boldsymbol{k}_s)\right|^2}{\left|\boldsymbol{E}^i(\boldsymbol{k}_i)\right|^2} \right], \tag{57}$$

where $\boldsymbol{E}^i(\boldsymbol{k}_i)$ is the electric field of incidence plane wave in $\boldsymbol{k}_i$ direction and $\boldsymbol{E}^s(\boldsymbol{k}_s)$ is the electric field of the scattered wave in $\boldsymbol{k}_s$ direction, measured at a distance r of the target.

The multilayer structure (Figure 4) containing dipoles that their length and with are equal to 50 mm and 1 mm, respectively, is used to evaluate the *SCS* parameter. The dipole length is oriented along the x-direction while its width is oriented along the y-direction. For *SCS* analysis a basis structure characterized by $\varepsilon_r = 2.33$, $\text{tg}\delta = 1.2\times10^{-1}$, $\ell = 50$ cm, $\varepsilon_{rg} = 5$ and $\text{tg}\delta_g = 2.0\times10^{-1}$ is used. The evaluation, conducted at 1.25 GHz, uses a vertically polarized incident wave at oblique direction defined by $\theta_i = 40°$ and $\phi_i = 60°$. The *SCS* analysis comprises the influence of the inner layer by varying its thickness (ℓ) and its relative permittivity (ε_r). The *SCS* resulting curves are plotted in azimuth (θ_s fixed at θ_i and ϕ_s ranging from −180° to +180°) and in elevation (θ_s ranging from −90° to +90° and ϕ_s fixed at ϕ_i) directions. It is important to mention that for each analysis the others structure parameters were kept constant.

The plots of azimuth *SCS* for the ℓ variation are depicted in Figure 7. It can be observed that the *SCS* results for the structure containing the electric dipole are greater than those for the magnetic one. An inversion of the greatest and the lowest *SCS* curves, relative to both structures, is also observed in Figure 7. That is, for instance, the $\ell = 0.2\lambda_0$ leads to the greatest *SCS* values for the structure having the electric dipole, however conduct to the lowest *SCS* values for the structure with the magnetic dipole. From Figure 7b it can be seen that the greatest *RCS* level occurs when $\ell = 1.0\lambda_0$ and the ℓ values $0.1\lambda_0$, $0.2\lambda_0$, and $0.5\lambda_0$ present the lowest *RCS* levels, where the scattering of the dipole seems to be mandatory. The amplitude of the *SCS* variation (it is about 4 dB) is similar for both structures.

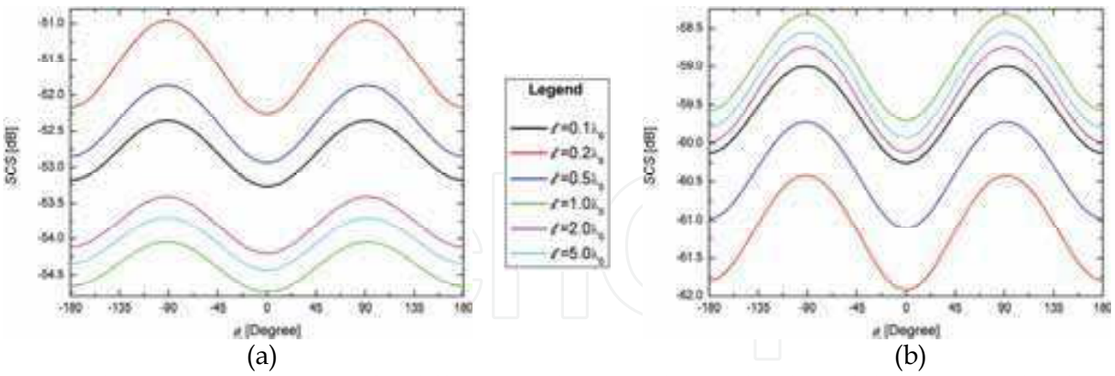

(a) (b)

Fig. 7 – The azimuth *SCS* curves for different ℓ values: (a) electric dipole and (b) magnetic dipole.

The effects of the inner layer relative permittivity (ε_r) on the *SCS* curves are shown for structure with electric dipole in Figure 8 and for structure that has the magnetic dipole in Figure 9. In both figures are presented the *SCS* in azimuth and elevation directions. In general, similarly to ℓ variation, the *SCS* values for the structure having the electric dipole are greater than those for the magnetic dipole. For the structure with the magnetic dipole is noted that there is not alteration in the curves shape, only in their *SCS* levels. These *SCS*

levels increase when the ε_r grows. However, the *SCS* curves shape as well as their magnitudes for the structure having the electric dipole are modified by the inner layer ε_r. From the azimuth *SCS* curves (Figures 8a and 9a) it can be seen that, for ε_r values greater than 4, the curves seem to show a kind of complementary. Since, in the ϕ_i angles where occur the maximum *SCS* levels for structure containing the electric dipole are found the minimum *SCS* level for the other structure and vice-versa. The *SCS* is sensitive to electromagnetic properties of the scattering element since; in general, both dipoles bring different responses.

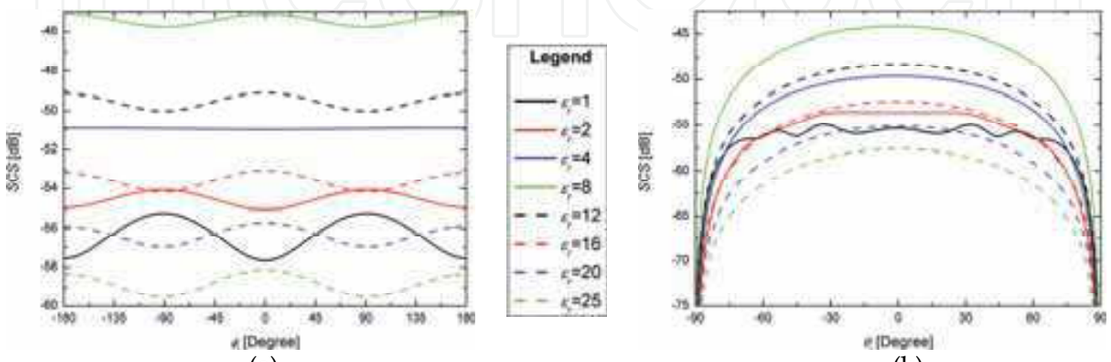

(a) (b)

Fig. 8 – The electric dipole *SCS* curves for different of ε_r values: (a) azimuth and (b) elevation.

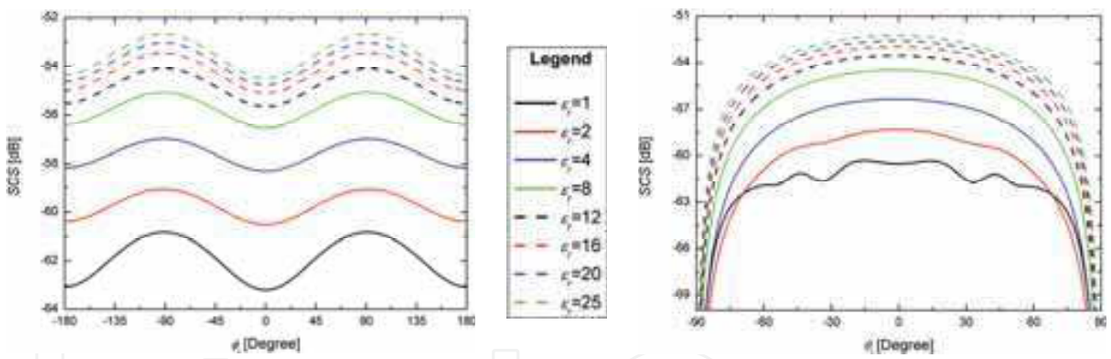

(a) (b)

Fig. 9 – The magnetic dipole *SCS* curves for different of ε_r values: (a) azimuth and (b) elevation.

Several parameters have been proposed to assist the interpretation and the classification of polarimetric SAR data. For instance, the entropy, the anisotropy and α–angle derived from Cloude-Pottier's target decomposition theorem (Cloude & Pottier, 1997) has been widely used for this purpose. The α–angle can be also used as characterization parameter since it provides information about the type of scattering mechanism. In this way, the α–angle was evaluated at 1.25 GHz for the same multilayer structure used on the *SCS* analysis. In Figure 10 is showed the α–angle variation in terms of the inner layer relative permittivity (ε_r).

From the evaluation of α–angle it is verified that the average α–angle varies completely different from that expected with α–theoretical (around 45°). This fact it is observed for both structures. It probably occurs due to the existence of cross components in the scattering matrix of the structures. In contrast, the computed α–dominant values are almost constant

and very close to 45° and to 60° for the structure containing the electric dipole and magnetic one, respectively. Therefore, according to (Cloude & Pottier, 1997), the scattering mechanism of the structure having the magnetic dipole can not be assumed as a scattering mechanism produced by an electric dipole. It leads to state that the layers introduce a certain degree of anisotropy to scattering mechanism of the magnetic dipole since its α–dominant value is characteristic of anisotropic scatter.

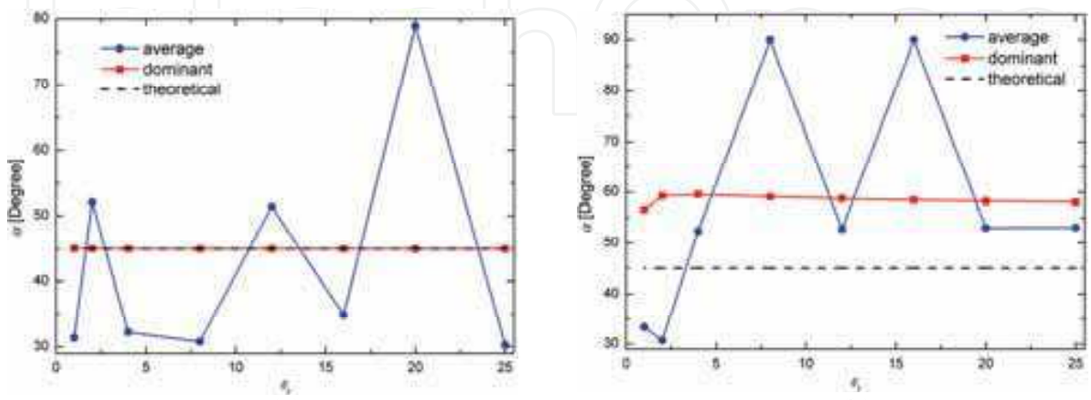

(a) (b)

Fig. 10 – The α–angle variation in terms of ε_r for structure with: (a) electric and (b) magnetic dipoles.

According to (van Zyl et al., 1987) the polarimetric response is another way to represent the target *SCS*. In this graphical representation, the *SCS* is plotted in function of ellipticity and orientation angles of the transmitted electromagnetic wave. The polarimetric responses for the multilayer structures containing the electric and the magnetic dipoles when $\varepsilon_r = 25$ are presented, respectively, in Figures 11 and 12. The polarimetric response is sensitive to electromagnetic properties of the scattering element since both dipoles bring different responses. Besides, it can be observed that the two polarimetric responses seem to be complementary, because the point where occurs the maximum value of polarimetric response for one dipole corresponds to the point of minimum value for the other dipole. This complementary relation can be though as the duality that there exist for both dipoles. The magnitude of the polarimetric response for electric dipole is greater than for the magnetic one for this value of ε_r, as can be sustained by Figures 8 and 9.

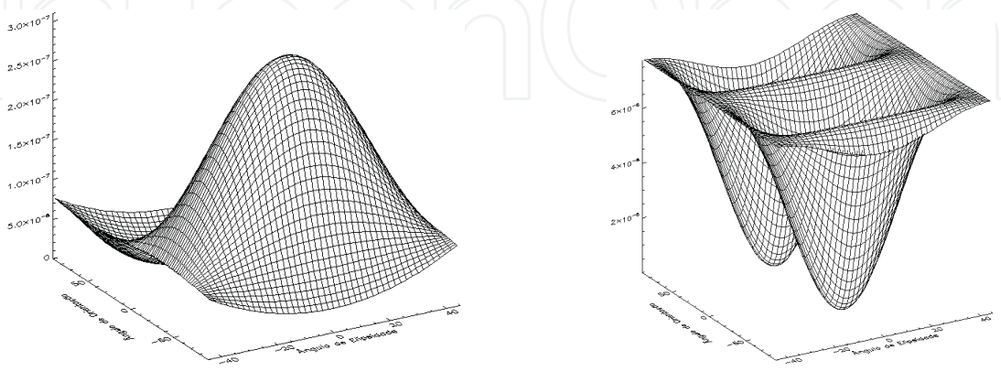

(a) (b)

Fig. 11 – Polarimetric response of electric dipole: (a) co-polarized and (b) cross polarized.

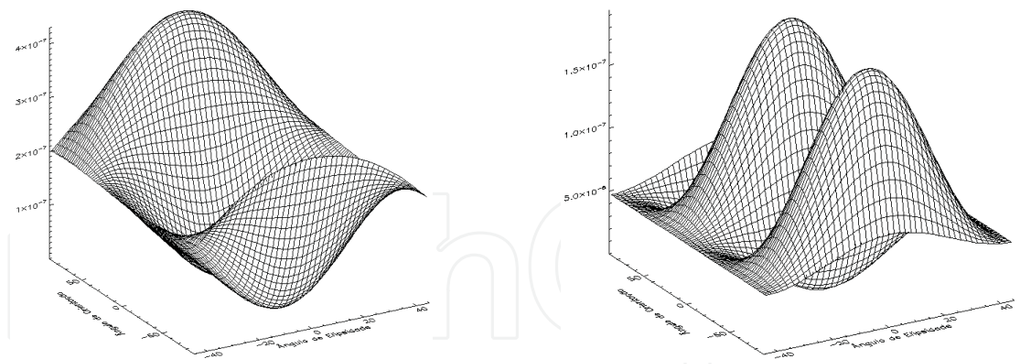

(a) (b)

Fig. 12 – Polarimetric response of magnetic dipole: (a) co-polarized and (b) cross polarized.

3.3 Polarimetric SAR Images Simulation

The polarimetric SAR data simulation is the third remote sensing application that is considered in this work, which can be derived from the current electromagnetic modeling. The methodological approach employed on the polarimetric SAR image simulation is completely described in (Sant'Anna et al., 2008b and Sant'Anna, 2009). It is based on the computation of the far electric field scattered by a multilayer structure excited by an elliptically polarized plane wave, in order to perform the simulation process as realistic as possible.

The multilayer structure used to simulate two sets of polarimetric SAR images is composed of three isotropic, linear and homogenous layers stacked up in z direction, as depicted in Figure 4. A rectangular perfect electric dipole, sizing 50×1 mm, is printed on the planar interface between the free space and the inner layer (interface $z = \ell$). This dipole has infinitesimal thickness and will act as scattering element. A large number of dipoles is spread over the inner layer in such way that is guaranteed at least 30 elementary scatters (dipoles) inside of each SAR resolution cell and there is no dominant scatter in the scene. The dipoles position and local orientation are conveniently (uniformly) distributed over the inner layer.

The simulated images represent the acquisition of an airborne monostatic SAR flying at 6000 m of height, having a grazing angle of 35º and imaging a terrain where only a small area of 290 × 290 m will be consider in the simulation. The simulated images were generated having 3.0 m of spatial resolution in range and azimuth directions and 2.8 m of pixel spacing in both directions. The SAR spread point function was represented by a separable two-dimensional sinc function, whose support region is a square window of 9×9 pixels.

The first image set, illustrated in Figure 13, was generated for a SAR operating at L-band (1.25 GHz) and for a multilayer structure having the following characteristics: the ground layer with relative permittivity $\varepsilon_{rg} = 5.0$ and loss tangent $\tan\delta_g = 2.0\times10^{-1}$, the inner layer characterized by thickness $\ell = 527.63$ mm, relative permittivity $\varepsilon_r = 2.33$ and loss tangent $\tan\delta = 1.2\times10^{-4}$ and both layers having μ_0 as magnetic permeability. In this set, the images contain four distinct regions that are different by local orientation of the electric dipoles. The dipoles are preferentially oriented at 10º, 30º and 20º, respectively, for upper left, upper right and lower right regions, while for lower left region the dipoles are oriented totally random (TR). These regions are denoted by A, B, C and D letters, respectively. It is important to mention that the orientation is referred to the azimuth-axis (az) and the origin of the system

coordinate is located at image center. Note that the VH channel is not presented in Figure 13 because it is equal to HV one, due to reciprocity assumption framework.

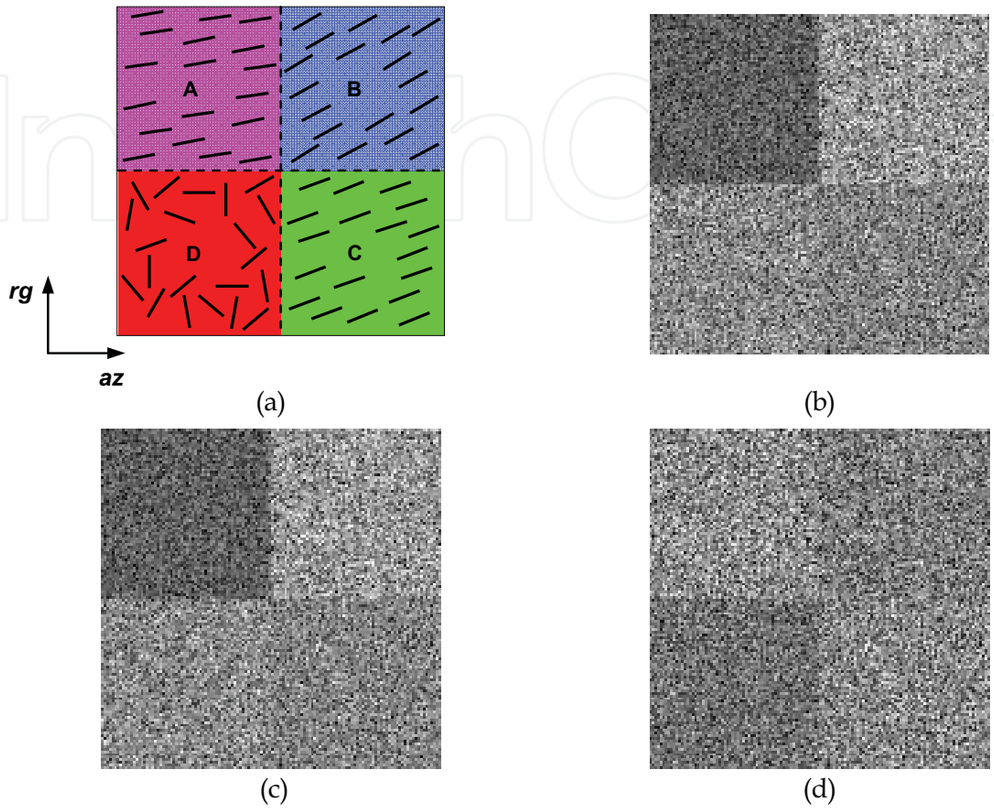

Fig. 13 – L-band amplitude simulated polarimetric SAR images: (a) Phantom, (b) HH, (c) HV and (d) VV channels.

These simulated SAR images were quantitatively evaluated in (Sant'Anna et al., 2008c). The amplitude SAR data were investigated by fitting a simple linear regression model to sixteen samples of 100×100 pixels extracted from each region. The polarimetric analysis was based on the discriminatory capability of the α and β angles derived from the standard Cloude-Pottier's decomposition theorem (Cloude & Pottier, 1997) and the orientation angle (φ) induced by azimuthal terrain slope (Lee et al., 2000).

Under linear detection and for single look data the ratio of the standard deviation and the expected value (the coefficient of variation – C_v) over homogeneous area is constant and equal to $[(4-\pi)/\pi]^{1/2} = 0.5227$. This value can be obtained from the moments of the Rayleigh distribution. As consequence, a simple way of evaluating the simulated data is to check whether the mean value (μ) and the standard deviation (σ) of the data holds, within homogeneous area, the linear relationship $\sigma = 0.5227*\mu$. This analysis was performed by applying a simple linear regression model to the estimated means and standard deviations for all sixty four samples in each channel.

The adjusted linear model ($Y = b_0+b_1*X$) and expected one ($Y = 0.5227*X$) are depicted on Figure 14 in each channel, respectively, by dashed and solid lines. From the adjusted model,

where Y represents the standard deviations and X the mean value, is expected that the estimated intercept (b_0) and slope (b_1), should be zero and 0.5227, respectively. It can be noted that two straight lines are almost coincident, showing that the adjusted model and theoretical one are approximately equal.

A Student's t-test for the intercept being equal to zero and the slope being equal to 0.5227 was performed. These two parameters and their p-values for statistical analysis of the regression are shown in Table 1. The estimated slope values are around the expected value (0.5227) for all channels. The estimated intercept values for HH and VV channels are very close to 0, and for HV channel is a little bit higher than this value. Analyzing the p-values is observed that only one value lower than 5% is encountered for b_1 test in VV channel, that is, for this case there is no evidence to accept the hypothesis of b_1 to be equal to 0.5227 at 95% of significance level.

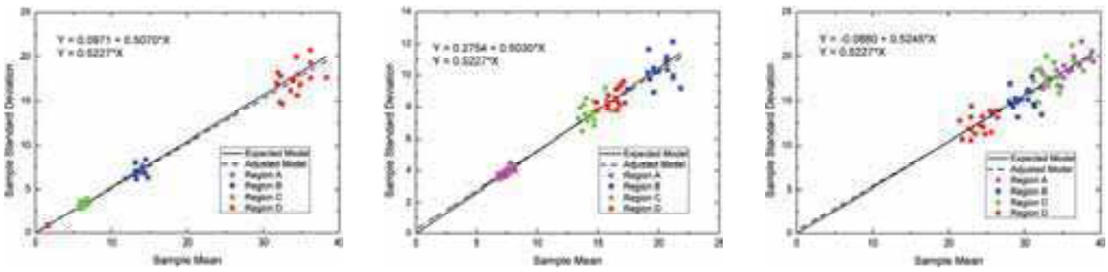

(a) (b) (c)

Fig. 14 – Linear fit to sample data: (a) HH, (b) HV and (c) VV channels.

Channel	b_0	b_1	p-value*100%	
			b_0	b_1
HH	0.0971	0.5070	47.34	94.24
HV	0.2754	0.5030	70.98	75.12
VV	-0.0880	0.5245	6.74	4.40

Table 1. Statistics for the linear regression fit.

From the linear fit results it can be concluded that the polarimetric SAR data has one look and the regions can be considered as homogeneous areas. Additionally, the equivalent number of looks (*ENL*) was estimated for the whole image based on all the sixty-four samples. The estimated *ENL* for the HH, HV and VV channels are 1.005, 0.994 and 0.998, respectively, which results in 0.999 as final estimate of *ENL* computed as mean of those individual estimates. The estimated values are very close to one, as expected for a single look data.

Knowing that the α-angle provides information about the scattering mechanism and the β and φ angles are related to target orientation angle, it was formed attributes bands from pointwise estimation of these angles. The α, β and φ images and their respective histograms are shown in Figure 15.

The α image does not show a notably difference among the image regions, leading to a low discriminatory capability based on only α feature. The α-angle mean value of each region is around 55.96°, value that is greater than 45° (typical value for electric dipole scattering mechanism), it probably occurs due to the existence of cross components in the scattering matrix. Comparing the results presented in (Sant'Anna et al., 2007b), where the dipole

scattering was mandatory, it is concluded that the thickness of the inner layer can influences significantly in the scattering mechanism of the multilayer structure. Therefore, might be state that the inner layer can introduce a certain degree of anisotropy to scattering mechanism of the regions.

As abovementioned the difference among the regions comes from the dipole local orientation, in this sense is expected that β and φ angle images present, in general, the best discriminatory capability. This fact is easily verified by a visual inspection of Figures 15b and 15c, where the four image regions appear visually distinguishable. The β and φ image histograms exhibit three dominant modes that are related to the values of regions A, B and C. However, for these regions the variances of φ values are smaller than those of β values, meaning that the former image (φ) presents regions more homogeneous than the later one (β image), which displays an aspect noisier than φ image and this fact influences on the regions discrimination.

In order to evaluate the discriminatory capability of β and φ polarimetric features a simple threshold classification procedure was employed. The thresholds were defined based on the mean and one standard deviation of each region ($\mu_{reg}\pm\sigma_{reg}$, where *reg* stands for region). Over the classified images was applied a mode filter with window of 3×3 pixels to improve the classification results. The final classified images that arise from β and the φ images are illustrated in Figure 16. The classification performance was assessed from the matrix confusion (Tables 2 and 3), overall accuracy and kappa coefficient of agreement and its sample variance. The confusion matrices were estimated based on all pixels of each region.

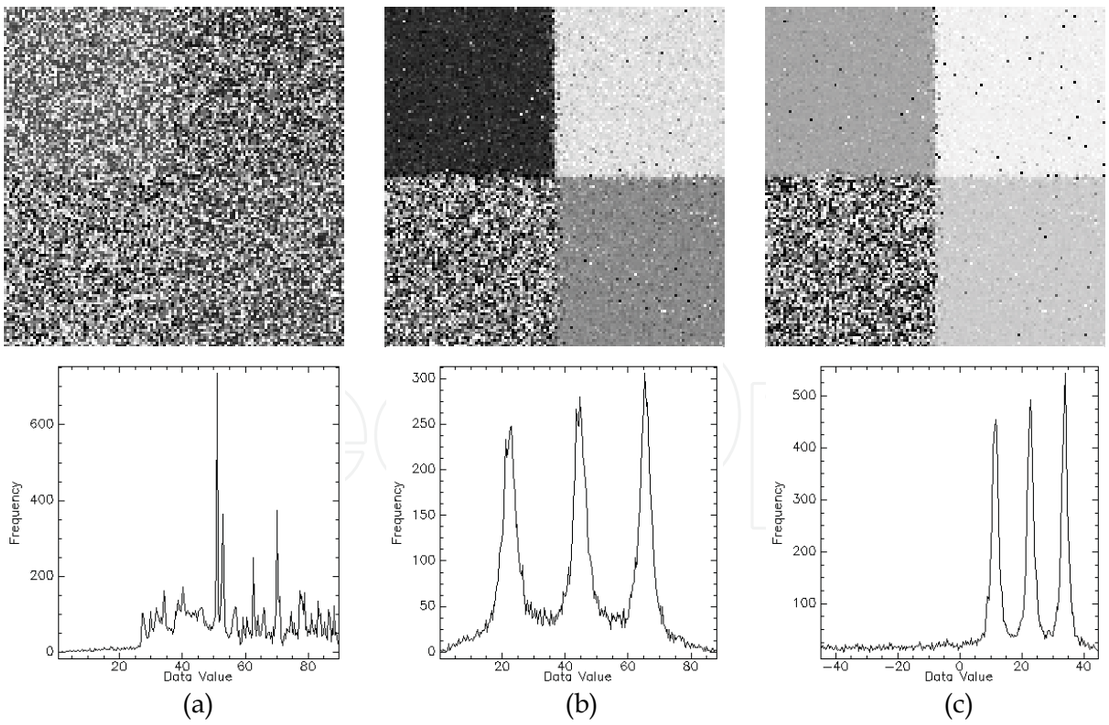

(a) (b) (c)

Fig. 15 – Angle images and their respective histograms: (a) α, (b) β and (c) φ.

In general, from Figure 16 can be noticed that all regions are better classified when the φ angles feature is used, this is corroborated by the values of overall accuracy and kappa coefficient. From a statistical z-test with 95% of significance level is observed that the classification result of φ image is much better than that obtained with β image, showing that discriminatory power carried by φ feature is superior to one gathered by β feature, for the simulated image used in this study. It is noted that the regions border are better defined in φ image classification, probably due to their smallest class variances.

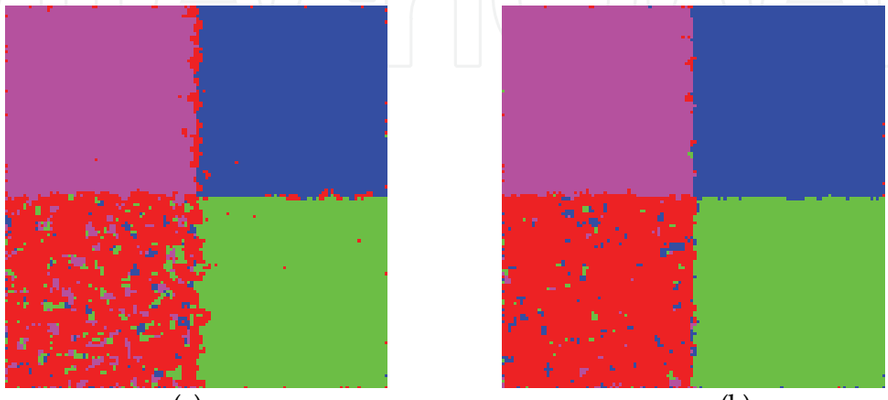

(a) (b)

Fig. 16 – Classified images arising from: (a) β and (b) φ features.

Orig./Class	A	B	C	D
A	96.22	0.02	0.05	3.71
B	0.03	97.34	0.07	2.56
C	0.00	0.15	96.85	3.00
D	8.69	3.66	7.86	79.79
Overall Accuracy = 0.93				
$\hat{\kappa} = 0.90$ and $\hat{\sigma}^2_{\kappa} = 7.46 \times 10^{-6}$				

Table 2. Confusion matrix for β image.

Orig./Class	A	B	C	D
A	97.80	0.17	0.12	1.91
B	0.05	99.76	0.02	0.17
C	0.07	0.95	98.10	0.88
D	1.54	4.39	0.98	93.09
Overall Accuracy = 0.97				
$\hat{\kappa} = 0.96$ and $\hat{\sigma}^2_{\kappa} = 2.97 \times 10^{-6}$				

Table 3. Confusion matrix for φ image.

The region D, where dipole local orientation angles are randomly distributed, presents the greatest confusion in both classification results, being the worst classified region. The region B (dipole oriented preferentially at 30°) obtained the best region discrimination. The regions A (dipoles at 10°), B and C (dipoles at 20°) are very well differentiate by the simple threshold method, using β and φ features. The β image classification is characterized by the largest misclassification of the region D values. The classification results point out that these two features gather the proper information to distinguish targets whose present differences in their scatter orientation about the radar line sight.

The variation of the soil moisture content might be symbolized by variations on the relative permittivity and on the loss tangent of the structure layers. As consequence, simulated images containing regions that are distinct by these layers dielectric parameters should be used aiming for the retrieval of soil moisture from SAR data studies. Keeping this idea in mind the second image set was generated. Images having five different regions were simulated for a SAR operating at C-band (5.3 GHz) and X-band (9.6 GHz). The dielectric parameters of the multilayer structure of each image region are presented in Table 4.

Using the HH and VV images were computed two polarimetric attributes derived from the backscattering coefficient. The former was proposed in (Singh & Dubey, 2007) and is called by polarization discrimination ratio (*PDR*). The later was employed in (Tadono et al., 1999) and is denoted here as polarimetric description square root (*PDS*). These attributes are, respectively, given by

$$PDR = \frac{\sigma_{vv}^0 - \sigma_{hh}^0}{\sigma_{vv}^0 + \sigma_{hh}^0}, \tag{58}$$

$$PDS = \sqrt{\sigma_{vv}^0 \, \sigma_{hh}^0}, \tag{59}$$

where σ_{pq}^0 represents the backscattering coefficient for *pq* polarization.

Region Location	ε_r	$\tan\delta_r$	ε_{rg}	$\tan\delta_g$	Dipole Orientation
Upper Left	2.33	1.2×10^{-4}	5.0	2.0×10^{-1}	10^o
Lower Right	2.33	1.2×10^{-4}	5.0	2.0×10^{-1}	30^o
Central	2.33	1.2×10^{-4}	5.0	2.0×10^{-1}	TR(a)
Lower Left	4.00	1.2×10^{-1}	8.0	$2.0\times10^{+1}$	TR
Upper Right	2.33	1.2×10^{-4}	8.0	$2.0\times10^{+1}$	TR

(a) TR means totally random.

Table 4. Dielectric characteristic of the structure layers of each image region.

The attribute images are depicted in Figures 17 and 18 for C- and X-bands, respectively. In these figures are also shown their respective *ICM* (Correia et al., 1998) classification results. It is important to mention that it was assumed a bivariate Gaussian distribution to model the joint density of the *PDR* and *PDS* attributes. From the classification results it can be noted that the five image regions were completely distinguished in both bands. The overall accuracy reached 99.75% for C-band images and 99.70% for X-band images, showing that the *PDR* and *PDS* attributes properly combined can be used to discriminate image regions having different dielectric characteristics.

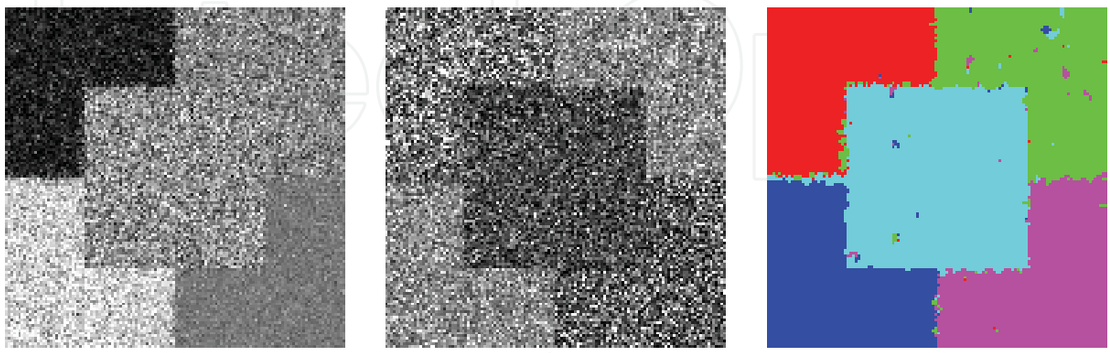

(a) (b) (c)

Fig. 17 – C-band images: (a) *PDR*, (b) *PDS* and (c) classified.

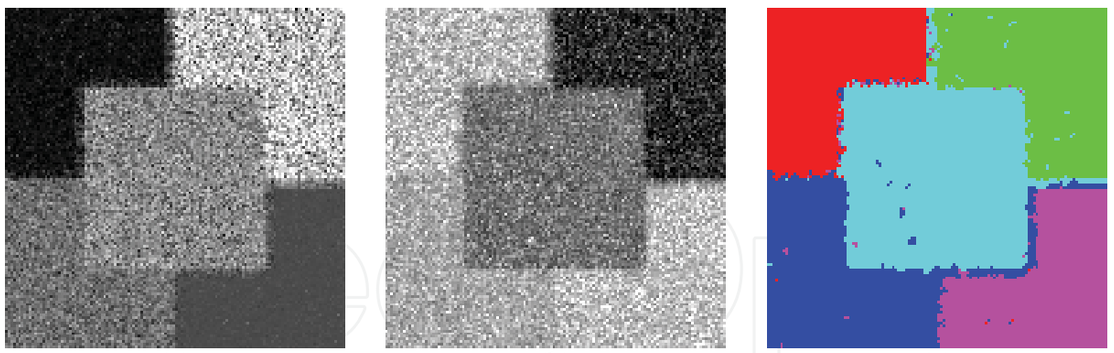

(a) (b) (c)

Fig. 18 – X-band images: (a) *PDR*, (b) *PDS* and (c) classified.

4. Conclusions

A scattering electromagnetic model for planar multilayer structure is introduced in this work. The methodological approach used to determine the electromagnetic fields existing in this type of structure is concisely described. The electromagnetic model potentiality is demonstrated through some remote sensing applications. These applications include the establishment of analytical expression for the scattering matrix of electric and magnetic dipoles, the simple target electromagnetic characterization and the 1-look SAR polarimetric image simulation.

The characterization of radar scattering from complex targets in terms of a linear combination of scattering from simpler ones, consists in an effective tool for the analysis of polarimetric data. From this point of view, knowledge of the scattering matrix from simpler targets is crucial to extract information gathered by polarimetric SAR data. Besides, the closer to the exact solution the determination of the scattering matrix is, the more precise the scattering analysis will be. From polarimetric SAR images and using the knowledge of scattering matrix it is possible, for instance, to develop mathematical models for natural targets and to derive several polarimetric target descriptors. It is also possible to improve the classification accuracy of land cover and use, to identify the scattering mechanisms intrinsic on an ensemble of pixels, and to built up a sensor calibration processes. In this context, the computation of scattering matrix plays a central rule in the polarimetric radar remote sensing imagery.

The scattering characterization of dipoles embedded in multilayer structure was carried out by evaluate the directivity function, the scattering cross section (*SCS*), the polarimetric response and the α–angle derived from Cloude-Pottier's target decomposition theorem. The directivity function revealed that the both infinitesimal dipoles irradiate differently, indicating their distinct electromagnetic nature. Besides, from the directivity function it could be the influence of the inner layer thickness on the radiated power. The *SCS* curves analysis demonstrated how the inner layer thickness (ℓ) and the relative permittivity (ε_r) of a multilayer structure can affect the target characterization. The ℓ parameter affects only the *SCS* levels while the ε_r influences the *SCS* shape as well as its level. In general, the *SCS* shape is dissimilar for the electric and magnetic dipoles. This statement is also verified from the graphic of polarimetric response. The estimated average α–angle for both dipoles showed great deviation from the theoretical one. On the other hand, when the dominant α–angle is used the estimative for the electric dipole is in accordance with expected one. However, for the magnetic dipole

the estimated dominant α–angle values are constant and greater than 45° (typical value for an electric dipole), indicating a degree of anisotropy in the scattering mechanism.
The developed image simulation process is not restricted to monostatic airborne sensors, it can be employed to orbital sensors as well as in bistatic configuration without any additional complexity. The simulated images can be generated at several operating frequencies, containing different spatial resolution and pixel spacing among others SAR parameters. The generated images were evaluated according to several measurements commonly employed in SAR data analysis. It was checked by using a simple regression linear model whether the mean value (μ) and the standard deviation (σ) of the data exhibit the linear relationship $\sigma = 0.5227 \times \mu$ within homogeneous areas. From regression linear analysis it can be concluded that this relationship holds for all simulated images. The equivalent number of looks was estimated, proving that the simulated data have only one look as simulated. It was also assessed the discriminatory capability of the image regions by applying two classification approaches, one using a simple threshold procedure and other based on the *ICM* classifier. Consequently, from the evaluation results it can be concluded that the simulation process is working properly, since the results are in accordance with those presented in the literature.
Furthermore this simulation process can be used to improve the understanding of SAR data properties in different situation, images can be generated to do theoretical as well as practical studies in several SAR subjects. From these kind of simulated image can be developed specific tools for digital image processing and to perform studies relative to SAR data calibration. In the remote sensing context still catches a glimpse the use of the model in ground penetrating radar (GPR) studies. Finally, from the obtained results it can be concluded that the presented electromagnetic model is a useful and powerful tool to be utilized in several remote sensing issues.

5. References

Balanis, C. A. (1997). *Antenna theory: analysis and design*. New York, John Willey & Sons Inc.

Cloude, S. R. & Pottier ,E. (1996). A review of target decomposition theorems in radar polarimetry. *IEEE Transactions on Geoscience and Remote Sensing*, Vol. 34, No. 2, 498-512.

Cloude, S. R. & Pottier E. (1997). An entropy based classification scheme for land applications of polarimetric SAR, *IEEE Transactions on Geoscience and Remote Sensing*, Vol. 35, No. 1, 68–78.

Collin, R. E. & Zucker, F. J. (1969). *Antenna Theory: Part 1*, New York, McGraw-Hill Book Company.

Correia, A. H.; Freitas,C. C.; Frery, A. C.; & Sant'Anna, S. J. S. (1998). A user friendly statistical system for polarimetric SAR image classification. *Revista de Teledetección*, Vol. 10, 79–93.

Freeman, A. & Durden, S. L. (1998). A three component scattering model for polarimetric SAR data. *IEEE Transactions Geoscience and Remote Sensing*, Vol. 36, No. 3, 963-973.

Institute of Electrical and Electronics Engineers (1993). *IEEE Std 145–1993: IEEE standard definitions of terms for antennas*. New York.

Israelsson, H.; Ulander, L. M. H.; Martin, T.; Askne, J. I. H. (2000). A coherent scattering model to determine forest backscattering in the VHF. *IEEE Transactions on Geoscience and Remote Sensing*, Vol. 38, No. 1, 238–248.

Lacava, J. C. S.; Proaño De la Torre, A. V. & Cividanes, L. (2002). A dynamic model for printed apertures in anisotropic stripline structures, *IEEE Transactions on Microwave Theory*, Vol. 50, No.1, 22–26.

Lee, J. S.; Schuler, D. L. & Ainsworth, T. L. (2000). Polarimetric SAR data compensation for terrain azimuth slope variation. *IEEE Transactions on Geoscience and Remote Sensing*, Vol. 38, No. 5, 2153-2163.

Lin, C. Y. & Sarabandi, K. (1999). A Monte Carlo coherent scattering model for forest canopies using fractal-generated trees. *IEEE Transactions on Geoscience and Remote Sensing*, Vol. 37, No. 1, 440–451.

Marin, M. A.; Barkeshli, S. & Pathak, P. H. (1990). On the location of proper and improper surface wave poles for the grounded dielectric slab. *IEEE Transactions on Antennas and Propagation*, Vol. 38, No.4, 570–573.

Newman, E. H. & Forrai, D. (1987). Scattering from microstrip patch. *IEEE Transactions on Antennas and Propagation*, Vol. AP–35, No.3, 245–251.

Sant'Anna, S. J. S., Lacava, J. C. S. & Fernandes, D. (2007a). Closed form expressions for scattering matrix of simple targets in multilayer structures, in *Proceedings of International Geoscience and Remote Sensing Symposium*, Barcelona, Spain, July 2007, 714–717.

Sant'Anna, S. J. S., Lacava, J. C. S. & Fernandes, D. (2007b). A useful tool to simulate polarimetric SAR images. *Proceedings of Eleventh URSI Commission F Triennial Open Symposium on Radio Wave Propagation and Remote Sensing*. Rio de Janeiro, Rio de Janeiro.

Sant'Anna, S. J. S., Lacava, J. C. S. & Fernandes, D. (2008a). Evaluation of the scattering matrix of flat dipoles embedded in multilayer structures. *PIERS Online*, Vol. 4, No. 5, 536–540.

Sant'Anna, S. J. S., Lacava, J. C. S. & Fernandes, D. (2008b). From Maxwell's equations to polarimetric SAR images: a simulation approach. *Sensor*, Vol. 8, No. 11, 7380–7409.

Sant'Anna, S. J. S., Lacava, J. C. S. & Fernandes, D. (2008c). Analysis of simulated polarimetric SAR images generated by a multilayer electromagnetic scattering model., *Proceedings of International Geoscience and Remote Sensing Symposium*, Boston, July 2008, 1245–1248.

Sant'Anna, S. J. S. (2009). Modelagem do espalhamento eletromagnético de estruturas multicamadas com aplicações em sensoriamento remoto por micro-ondas, *PhD. Thesis* (in Portuguese), ITA, São José dos Campos.

Singh, D. & Dubey, V. (2007). Microwave bistatic polarization measurements for retrieval of soil moisture using an incident angle approach, *Journal of Geophysics and Engineering*, n. 4, 75–82.

Tadono, T.; Qong, M.; Wakabayashi, H.; Shimada, M.; Kobayashi, T. & Shi, J. (1999). Preliminary studies for estimating surface soil moisture and roughness based on a simultaneous experiment with CRL/NASDA airbone SAR (PI–SAR), *Proceedings of Asian Conference on Remote Sensing*. Hong Kong.

Ulaby, F. T. & Elachi, C. (1990). *Radar polarimetry for geoscience applications.* Norwood, Artech House.

Yang, J.; Peng, Y. N. & Lin, S. M. (2001). Similarity between two scattering matrices, *Electronics Letters*, Vol. 37, No. 3, 193–194.

van Zyl, J. J.; Zebker, H. A. & Elachi, C. (1987). Imaging radar polarization signatures: theory and observation. *Radio Science*, Vol. 22, No. 4, 529-543.

Zurk, L. M.; Koistinen, P.; Sarvas, J. & Holmström, L. (2001). Electromagnetic scattering model for forest remote sensing. *Research Reports A38*, University of Helsinki, Helsinki.

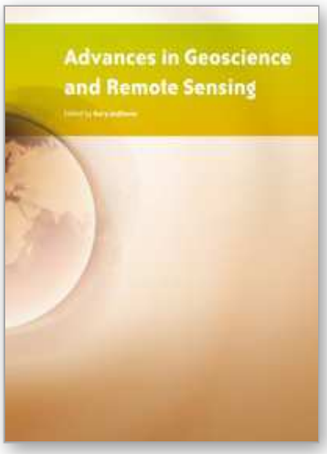

Advances in Geoscience and Remote Sensing

Edited by Gary Jedlovec

ISBN 978-953-307-005-6

Hard cover, 742 pages

Publisher InTech

Published online 01, October, 2009

Published in print edition October, 2009

Remote sensing is the acquisition of information of an object or phenomenon, by the use of either recording or real-time sensing device(s), that is not in physical or intimate contact with the object (such as by way of aircraft, spacecraft, satellite, buoy, or ship). In practice, remote sensing is the stand-off collection through the use of a variety of devices for gathering information on a given object or area. Human existence is dependent on our ability to understand, utilize, manage and maintain the environment we live in - Geoscience is the science that seeks to achieve these goals. This book is a collection of contributions from world-class scientists, engineers and educators engaged in the fields of geoscience and remote sensing.

InTech Europe
University Campus STeP Ri
Slavka Krautzeka 83/A
51000 Rijeka, Croatia
Phone: +385 (51) 770 447
Fax: +385 (51) 686 166
www.intechopen.com

InTech China
Unit 405, Office Block, Hotel Equatorial Shanghai
No.65, Yan An Road (West), Shanghai, 200040, China
中国上海市延安西路65号上海国际贵都大饭店办公楼405单元
Phone: +86-21-62489820
Fax: +86-21-62489821

IntechOpen